

Moiré-induced electronic structure modifications in monolayer V_2S_3 on Au(111)

Umut Kamber¹, Sahar Pakdel², Raluca-Maria Stan², Anand Kamlapure¹, Brian Kiraly¹, Fabian Arnold², Andreas Eich¹, Arlette S. Ngankeu², Marco Bianchi², Jill A. Miwa², Charlotte E. Sanders³, Nicola Lanatà², Philip Hofmann², Alexander A. Khajetoorians^{1}*

1. Institute for Molecules and Materials, Radboud University, Nijmegen 6525AJ, The
Netherlands

2. Department of Physics and Astronomy, Interdisciplinary Nanoscience Center, Aarhus
University, 8000 Aarhus C, Denmark

3. Central Laser Facility, STFC Rutherford Appleton Laboratory, Harwell, Didcot OX11 0QX,
United Kingdom

KEYWORDS: two dimensional materials, transition metal dichalcogenides, moiré, scanning tunneling microscopy, angle-resolved photoemission spectroscopy, density functional theory

ABSTRACT: There is immense interest in how the local environment influences the electronic structure of materials at the single layer limit. We characterize moiré induced spatial variations in the electronic structure of in-situ grown monolayer V_2S_3 on Au(111) by means of low temperature scanning tunneling microscopy and spectroscopy. We observe a long-range modulation of the

integrated local density of states (LDOS), and quantify this modulation with respect to the moiré superstructure for multiple orientations of the monolayer with respect to the substrate. Scanning tunneling spectroscopy reveals a prominent peak in the LDOS, which is shifted in energy at different points of the moiré superstructure. Comparing *ab initio* calculations with angle-resolved photoemission, we are able to attribute this peak to bands that exhibit a large out-of-plane *d*-orbital character. This suggests that the moiré driven variations in the measured density of states is driven by a periodic modulation of the monolayer-substrate hybridization.

INTRODUCTION

Moiré superstructures, constructed from monolayers of van der Waals (vdW) materials like graphene, have emerged as a tunable platform to artificially create novel quantum states of matter¹⁻⁵. As demonstrated for structures involving monolayer graphene, moiré interference can lead to long-range structural and electronic modulations, which can be imaged with scanning tunneling microscopy/spectroscopy (STM/STS) and low energy electron diffraction (LEED)^{6,7}. Such moiré superstructures, for example involving monolayer graphene, lead to various modifications of the band structure⁸, such as the minigap and replica band features observed in angle-resolved photoemission spectroscopy (ARPES)⁹. The moiré superstructure and its associated structural/electronic modifications can be quenched by decoupling the monolayer via intercalation, leading to quasi-free-standing electronic structure^{10,11}. As the family of tunable moiré materials grows¹²⁻¹⁵, it is important to understand how moiré superstructures can modify the structural, electronic, and magnetic properties of vdW monolayers at the atomic length scale.

One class of vdW materials, transition metal dichalcogenides (TMDs), have been synthesized at the monolayer limit on various surfaces leading to moiré superstructures¹⁶⁻²². In the case of TMDs

grown on metallic surfaces, strong interactions with the substrate, typically resulting from hybridization and modified charge screening, lead to pronounced modifications in the electronic structure^{23, 24}. For the MoS₂ monolayer on Au(111), these strong interactions lead to a renormalization of the band gap^{22, 25, 26} when compared to the quasi-free-standing case²⁷. Similarly, for the TaS₂ monolayer grown on Au(111), interactions with the underlying substrate suppress the expected charge density wave (CDW) phase^{16, 23, 28}, which can remain robust in TaS₂ monolayers prepared on other substrates²⁹. Yet, for many TMD monolayers where the moiré superstructure shows strong signatures in STM and LEED, the moiré superstructure minimally perturbs the band structure observed in ARPES^{16, 17}. Because many TMD monolayers show non-trivial electronic phases²⁹⁻³¹, it is important to study how long-range structural and electronic modifications induced by moiré superstructures modify the electronic structure.

Here, we study the structural and electronic properties of monolayer V₂S₃ on Au(111) to quantify the interplay between the moiré superstructure, the geometrical structure, and the electronic structure. Utilizing STM/STS, we observe well-defined, long-range modulations in constant-current imaging, i.e. the integrated density of states, reminiscent of a CDW. By investigating monolayer domains with varying rotation angle with respect to the Au(111) substrate, we confirm the persistence of these real-space modulations at all observed angles. Using detailed moiré simulations, we capture these modulations by considering higher-order wave vectors from the atomic lattice. Concomitantly, we use STS to identify a strong peak-like feature in the LDOS near E_F , which shifts in energy depending on the location within the moiré unit cell. In order to identify the peak seen in STS, we computed the band structure within density functional theory (DFT). By calibrating the effective doping using ARPES, we link the peak in the LDOS with the onset of weakly dispersing bands arising from the intrinsic V₂S₃ monolayer, with a substantial out-of-plane

orbital character. We suggest that the out-of-plane character of the V_2S_3 bands enables them to couple to the possible structural modulations of the moiré superstructure, inducing the observed spatial variations in the electronic structure.

RESULTS AND DISCUSSION

Characterization of the atomic structure of the V_2S_3 monolayer is shown in Figure 1 using high-resolution constant-current imaging. A two-fold symmetric structure of the top-layer S atoms is visible; within this layer, the S atoms form a rectangular unit cell (\mathbf{a}, \mathbf{b}) with two S (red and gray atoms in Figure 1d) atoms along \mathbf{b} , while the bottom S layer (pink atoms in Figure 1d) maintains a configuration similar to that of VS_2 . The atomically resolved constant-current image in Figure 1c reveals a unit cell with lattice constants $|\mathbf{a}| = 0.31 \pm 0.03$ nm and $|\mathbf{b}| = 0.87 \pm 0.03$ nm. The unit cell of the V_2S_3 is indicated with a dashed green rectangle in Figure 1c, which is consistent with the model in Figure 1d, determined using room-temperature STM and X-ray photoelectron diffraction³².

Concurrently with the atomic structure, additional longer-range modulations can be seen in constant-current imaging. Examining a fast Fourier transform (FFT) of the image in Figure 1a (Figure 1b), we observe many well-defined peaks corresponding to long-range features observed in real space (the reciprocal space points of the atomic lattice are highlighted by green circles). In constant-current images, a weaker moiré superstructure was observed compared to TMD layers grown on Au(111)^{16, 22}. We label the first-order features in reciprocal space, namely, the largest real-space periodicities that are responsible for the observed moiré superstructure, A and B. In addition to these features, we also observe periodic modulations in constant-current imaging with characteristic real-space length scales longer than the atomic lattice, yet smaller than the moiré lattice. These multiple higher-order features are also visible in the FFT, two of which we label C

and D (comprised of linear combinations of A, and B). While higher order features related to the moiré superstructure are often visible in LEED for families of sulfide-based TMDs grown on Au(111), there are commonly no strong indications of such higher order features in STM measurements in contrast to what is observed here¹⁶. Yet for V_2S_3 on Au(111), LEED measurements were not able to identify a moiré superstructure or any related higher-order features³².

To further study these higher order features, we characterized different orientations of the V_2S_3 layer with respect to the substrate using atomic resolution imaging. In Figure 2a, the stacking angle between \mathbf{a} and the $\langle 110 \rangle$ directions of Au(111) is $\theta = 0^\circ$, measured by comparing the atomic lattice of V_2S_3 with the herringbone reconstruction of underlying Au(111). Two other monolayer islands with measured rotation angles of $\theta = 1.3^\circ \pm 0.5^\circ$ and $\theta = 4.2^\circ \pm 1.0^\circ$ are shown in Figure 2b and Figure 2c. However, approximately 80% of the observed V_2S_3 islands were aligned with the stacking angle of $\theta = 0^\circ$ (forming three rotational domains at 120° with respect to each other consistent with the three-fold symmetry of the Au(111) substrate), indicating that there is a preferred growth orientation for the V_2S_3 monolayer on Au(111) (see Supporting Information Figure S2). As seen in the FFTs in Figure 2d-f, both moiré superstructures and higher-order features are also present in the misaligned cases.

To understand the origin of the observed higher-order features and how these features relate to the geometrical influence of the moiré superstructure, we simulated the expected moiré superstructures by representing the top S layer of V_2S_3 and the topmost Au(111) layer as sinusoidal functions, and multiplying them using a rotation angle defined as the angle between \mathbf{a} and $\langle 110 \rangle$ ³³. We used higher-order sinusoidal functions for each lattice to visualize all the possible higher-order moiré modes (see Supporting Information section 1 for details). The resulting FFT of the

simulations and their corresponding real space data are shown in Figure 2g-i for each observed moiré superstructure. Our simulations successfully reproduce all of the reciprocal space features for the $\theta = 0^\circ$ moiré superstructure, as well as nearly all the features in the rotated cases when we include higher-order functions for both V_2S_3 and Au(111) (Figure 2g). Thus, we can confirm that the longer-range features observed in constant-current imaging stem from structural variations in the film.

To study local modifications in the electronic structure, we performed STS at different positions within the moiré superstructure (Figure 3). A signature of the V_2S_3 monolayer is a distinct peak near E_F . We observe that the position of this peak strongly varies depending on the spatial location within the moiré superstructure, as seen in dI/dV spectra taken on the apparent moiré minima (light blue) and apparent moiré maxima (dark blue) in Figure 3 (see also Supporting Information Figure S4). This can also be seen in spatially dependent maps of the differential conductance near the Fermi energy, leading to complex patterns (see Supporting Information Figure S3). By contrast, peak-like features seen in the LDOS for $TaS_2/Au(111)$ do not show significant shifts in energy within the moiré superstructure²³. On the other hand, moiré induced modifications to the LDOS were observed in monolayer MoS_2 on Au(111), in particular energy ranges, which the authors attributed to possible differences in hybridization or electronic screening³⁴. We suggest that the shifts in energy of the LDOS peak-like feature (Figure 3) may result from different hybridization strengths associated with the orbital character of the bands in this energy range; as shown in Figure S5, the orbital character contains an out-of-plane component that may be sensitive to the variations in interlayer distance between the monolayer and the substrate.

To elucidate the electronic properties of the system, including the origin of the observed peak in the LDOS, we performed DFT calculations of the free-standing monolayer V_2S_3 . In Figure 4a, we

show both the calculated band structure along the high-symmetry path indicated in the inset and the total DOS (Figure 4b) of the free-standing monolayer V_2S_3 . In order to account for the doping induced by the substrate, we shifted the calculated Fermi energy by assuming a rigid offset. By comparing the ARPES spectra with the monolayer DFT bands (Fig. 4a-c) at the Γ point and the Fermi contour (Fig. 4d), we observed that a satisfactory agreement is obtained by shifting the DFT bands by about 180 meV-220 meV. We note that in Figure 4 the theoretical Fermi level E_F (DFT) is lowered by 180 meV, and we refer to such shifted Fermi level as E_F (Exp). The comparison between the experimental and theoretical constant energy contours (including three 120° rotations corresponding to the three experimental domain rotations) with this offset Fermi level (E_F (Exp)) is shown in Figure 4d (see also Supporting Information Figure S6). The photoemission process is highly dependent on matrix elements; thus, not all features predicted by theory are visible in the ARPES data. However, the main qualitative features of the measured energy contours (EC) are captured by the DFT calculations. Further details of EC are discussed in the supplemental material.

Comparing the calculated total DOS (Figure 4b) to the observed peak in STS (Figure 3), we find good agreement. The calculated DOS of the native monolayer in Figure 4b contains sharp features at the shifted Fermi level, similar to features that are observed in dI/dV measurements in Figure 3. To understand the orbital texture of the bands contributing to the calculated DOS features at E_F (Exp), we projected the total DOS onto the vanadium d -orbitals (see Supporting Information Figure S5). From this decomposition, it emerges that these peaks in the total DOS have a substantial contribution from orbitals with out-of-plane character. We suggest that such out-of-plane orbital character may make the bands more susceptible to influence from the physical corrugation of the monolayer due to the moiré superstructure. The moiré superstructure can modify the hybridization of the monolayer bands with the substrate by varying the interlayer distance,

resulting in the observed shift in the peak position in Figure 3. As this behavior was also observed on misaligned moiré superstructures (Figure 3b), it appears to be related to the physical corrugation of the monolayer.

Both CDWs and magnetism have been observed in other V-based TMDs³⁵⁻³⁹ and predicted in VS₂⁴⁰⁻⁴². At temperatures down to 1.3 K, the enhanced DOS peak near E_F is consistently observed, in contrast with common expectations of a minimum in the DOS near the Fermi level in CDW systems. In order to investigate the interplay between the electronic and orbital degrees of freedom in our moiré system, we calculated the nesting function and the electronic susceptibility of the free-standing monolayer V₂S₃ (see Supporting Information section 5). Interestingly, both of these functions display a peak in the vicinity of one of the second-order reciprocal-space points of the moiré superstructure (indicated as the C-point in Figure 1, and Figure S7). This suggests the possibility of a connection between the formation of the moiré superstructure and the underlying electronic instabilities of the free-standing layer in this system. However, from this calculation alone, we cannot draw any direct conclusion concerning this point. Likewise, in order to draw any experimental conclusions about the tendency toward CDW formation, further work involving temperature-dependent STM measurements is required.

CONCLUSIONS

In conclusion, we studied the electronic structure of monolayer V₂S₃ grown on Au(111). Constant-current imaging revealed long-range modulations persistent at various rotation angles; as these modulations were captured in moiré simulations, they were attributed to higher-order modes from the moiré superstructure. Tunneling spectroscopy revealed a strong peak feature in

the LDOS near E_F , whose energy varied depending on the position within the moiré superstructure. Using ARPES, in conjunction with DFT calculations, we were able to relate the observed peak in STS to V_2S_3 bands with hybridization effects mainly due to the out-of-plane vanadium d -orbitals. We suggest that the moiré induced modulation of this peak could be due to coupling between the out-of-plane band character and the physical moiré corrugation. Future measurements on the temperature dependent evolution of the system could provide valuable insight into the interplay between the moiré modulated electronic structure and possible electronic instabilities in this material.

METHODS

Sample Preparation. V_2S_3 samples were prepared in-situ by the method described previously³². A clean Au(111) surface was first prepared by sputtering Ar^+ (1.5 kV) ions and subsequent annealing at 600 °C. Vanadium was then deposited by e-beam evaporation onto the substrate, which was held at room temperature. Following the deposition, the sample was annealed to $T = 450$ °C in an atmosphere of $p = 5 \times 10^{-5}$ mbar H_2S partial pressure, yielding monolayer VS_2 . V_2S_3 was then obtained by annealing the VS_2 to $T = 600$ °C at $p < 1 \times 10^{-9}$ mbar. The samples were in-situ transferred into the STM without breaking vacuum.

STM/STS measurements. All STM/STS measurements were performed under ultrahigh vacuum conditions with home-built low-temperature setup, operating at a base temperature of $T = 1.3$ K and 4.2 K, with the capability of applying a magnetic field perpendicular to the surface up to $B = 9$ T⁴³. All STM images in the main text and the Supporting Information were acquired by using constant-current feedback with the bias applied to the sample (V_s). Electrochemically etched tungsten (W) tips were used after in-situ treatment by electron bombardment. dI/dV measurements

were performed using a lock-in technique with a modulation bias (V_{mod}) at a frequency (f_{mod}) of 880 Hz added to the bias signal. Fast Fourier transforms of the real space STM images were calculated using MATLAB software. All the FFT images shown in this study have minimum 0.41 nm⁻¹/pixel resolution.

ARPES measurements. All ARPES measurements were acquired using a photon energy of 94 eV at the SGM3 endstation of the ASTRID2 synchrotron light source in Aarhus, Denmark. The energy and angular resolution were better than 40 meV and 0.2°, respectively⁴⁴.

DFT calculations. The DFT calculations were performed using the Vienna *ab initio* Simulation Package (VASP) code^{45, 46}. The exchange–correlation potentials were described through the Perdew–Burke–Ernzerhof (PBE) functional within the generalized gradient approximation (GGA) formalism⁴⁷. A plane wave basis set was used with a cutoff energy of 400 eV on a 7 x 21 Monkhorst-Pack k-point mesh⁴⁸. Lattice constants reported by Arnold *et.al*³² was used as the reference and was modified less than 10% to achieve a commensurate moiré lattice with the Au(111) substrate. A vacuum region of 25 Å along the z direction was used in order to minimize the interaction between the periodic repetitions of the cell.

ASSOCIATED CONTENT

Supporting Information

Details of the moiré simulations, additional real space characterization by STM and STS, DFT calculations for projected DOS of the *d*-orbitals of vanadium, additional ARPES results, and calculated electronic susceptibility of the free-standing monolayer V₂S₃.

AUTHOR INFORMATION

Corresponding Author

Alexander A. Khajetoorians - Institute for Molecules and Materials, Radboud University, Nijmegen 6525AJ, The Netherlands; Email: a.khajetoorians@science.ru.nl

Author Contributions

The manuscript was written through contributions of all authors. All authors have given approval to the final version of the manuscript.

ACKNOWLEDGMENT

B.K. acknowledges NWO-VENI project “Controlling magnetism of single atoms on black phosphorus” with project number 016.Veni.192.168. S.P. acknowledges support from Spanish MINECO for the computational resources provided through Grant FIS2016-80434-P. A.K. and A. A. K. acknowledges the VIDI project: “Manipulating the interplay between superconductivity and chiral magnetism at the single atom level” with Project No. 680-47-534, which is financed by NWO. U.K., A.E., and A.A.K. acknowledge funding from NWO. A. A. K acknowledges support from the European Research Council (ERC) under the European Union’s Horizon 2020 research and innovation programme (Grant Agreement No. 818399, SPINAPSE). This work was supported by VILLUM FONDEN via the Centre of Excellence for Dirac Materials (Grant No. 11744). J.A.M. acknowledges financial support from the Danish Council for Independent Research, Natural Sciences under the Sapere Aude program (grant no. DFF-6108-00409), and from Aarhus University Research Foundation.

REFERENCES

1. Dean, C. R.; Wang, L.; Maher, P.; Forsythe, C.; Ghahari, F.; Gao, Y.; Katoch, J.; Ishigami, M.; Moon, P.; Koshino, M.; Taniguchi, T.; Watanabe, K.; Shepard, K. L.; Hone, J.; Kim, P., Hofstadter's butterfly and the fractal quantum Hall effect in moiré superlattices. *Nature* **2013**, *497* (7451), 598-602.
2. Hunt, B.; Sanchez-Yamagishi, J. D.; Young, A. F.; Yankowitz, M.; LeRoy, B. J.; Watanabe, K.; Taniguchi, T.; Moon, P.; Koshino, M.; Jarillo-Herrero, P.; Ashoori, R. C., Massive Dirac Fermions and Hofstadter Butterfly in a van der Waals Heterostructure. *Science* **2013**, *340* (6139), 1427.
3. Ponomarenko, L. A.; Gorbachev, R. V.; Yu, G. L.; Elias, D. C.; Jalil, R.; Patel, A. A.; Mishchenko, A.; Mayorov, A. S.; Woods, C. R.; Wallbank, J. R.; Mucha-Kruczynski, M.; Piot, B. A.; Potemski, M.; Grigorieva, I. V.; Novoselov, K. S.; Guinea, F.; Fal'ko, V. I.; Geim, A. K., Cloning of Dirac fermions in graphene superlattices. *Nature* **2013**, *497* (7451), 594-597.
4. Cao, Y.; Fatemi, V.; Demir, A.; Fang, S.; Tomarken, S. L.; Luo, J. Y.; Sanchez-Yamagishi, J. D.; Watanabe, K.; Taniguchi, T.; Kaxiras, E.; Ashoori, R. C.; Jarillo-Herrero, P., Correlated insulator behaviour at half-filling in magic-angle graphene superlattices. *Nature* **2018**, *556* (7699), 80-84.
5. Cao, Y.; Fatemi, V.; Fang, S.; Watanabe, K.; Taniguchi, T.; Kaxiras, E.; Jarillo-Herrero, P., Unconventional superconductivity in magic-angle graphene superlattices. *Nature* **2018**, *556* (7699), 43-50.
6. Marchini, S.; Günther, S.; Wintterlin, J., Scanning tunneling microscopy of graphene on Ru(0001). *Physical Review B* **2007**, *76* (7), 075429.
7. N'Diaye, A. T.; Coraux, J.; Plasa, T. N.; Busse, C.; Michely, T., Structure of epitaxial graphene on Ir(111). *New Journal of Physics* **2008**, *10* (4), 043033.
8. Yankowitz, M.; Xue, J.; Cormode, D.; Sanchez-Yamagishi, J. D.; Watanabe, K.; Taniguchi, T.; Jarillo-Herrero, P.; Jacquod, P.; LeRoy, B. J., Emergence of superlattice Dirac points in graphene on hexagonal boron nitride. *Nature Physics* **2012**, *8* (5), 382-386.
9. Pletikosić, I.; Kralj, M.; Pervan, P.; Brako, R.; Coraux, J.; N'Diaye, A. T.; Busse, C.; Michely, T., Dirac Cones and Minigaps for Graphene on Ir(111). *Physical Review Letters* **2009**, *102* (5), 056808.
10. Ulstrup, S.; Andersen, M.; Bianchi, M.; Barreto, L.; Hammer, B.; Hornekær, L.; Hofmann, P., Sequential oxygen and alkali intercalation of epitaxial graphene on Ir(111): enhanced many-body effects and formation of pn -interfaces. *2D Materials* **2014**, *1* (2), 025002.
11. Larciprete, R.; Ulstrup, S.; Lacovig, P.; Dalmiglio, M.; Bianchi, M.; Mazzola, F.; Hornekær, L.; Orlando, F.; Baraldi, A.; Hofmann, P.; Lizzit, S., Oxygen Switching of the Epitaxial Graphene–Metal Interaction. *ACS Nano* **2012**, *6* (11), 9551-9558.
12. Seyler, K. L.; Rivera, P.; Yu, H.; Wilson, N. P.; Ray, E. L.; Mandrus, D. G.; Yan, J.; Yao, W.; Xu, X., Signatures of moiré-trapped valley excitons in MoSe₂/WSe₂ heterobilayers. *Nature* **2019**, *567* (7746), 66-70.
13. Tran, K.; Moody, G.; Wu, F.; Lu, X.; Choi, J.; Kim, K.; Rai, A.; Sanchez, D. A.; Quan, J.; Singh, A.; Embley, J.; Zepeda, A.; Campbell, M.; Autry, T.; Taniguchi, T.; Watanabe, K.; Lu, N.; Banerjee, S. K.; Silverman, K. L.; Kim, S.; Tutuc, E.; Yang, L.; MacDonald, A. H.; Li, X., Evidence for moiré excitons in van der Waals heterostructures. *Nature* **2019**, *567* (7746), 71-75.
14. Ulstrup, S.; Koch, R. J.; Singh, S.; McCreary, K. M.; Jonker, B. T.; Robinson, J. T.; Jozwiak, C.; Rotenberg, E.; Bostwick, A.; Katoch, J.; Miwa, J. A., Direct observation of minibands in a twisted graphene/WS₂ bilayer. *Science Advances* **2020**, *6* (14), eaay6104.
15. Zhang, C.; Chuu, C.-P.; Ren, X.; Li, M.-Y.; Li, L.-J.; Jin, C.; Chou, M.-Y.; Shih, C.-K., Interlayer couplings, Moiré patterns, and 2D electronic superlattices in MoS₂/WSe₂ hetero-bilayers. *Science Advances* **2017**, *3* (1), e1601459.
16. Sanders, C. E.; Dendzik, M.; Ngankeu, A. S.; Eich, A.; Bruix, A.; Bianchi, M.; Miwa, J. A.; Hammer, B.; Khajetoorians, A. A.; Hofmann, P., Crystalline and electronic structure of single-layer TaS₂. *Physical Review B* **2016**, *94* (8), 081404.

17. Grønborg, S. S.; Ulstrup, S.; Bianchi, M.; Dendzik, M.; Sanders, C. E.; Lauritsen, J. V.; Hofmann, P.; Miwa, J. A., Synthesis of Epitaxial Single-Layer MoS₂ on Au(111). *Langmuir* **2015**, *31* (35), 9700-9706.
18. Dendzik, M.; Michiardi, M.; Sanders, C.; Bianchi, M.; Miwa, J. A.; Grønborg, S. S.; Lauritsen, J. V.; Bruix, A.; Hammer, B.; Hofmann, P., Growth and electronic structure of epitaxial single-layer WS₂ on Au(111). *Physical Review B* **2015**, *92* (24), 245442.
19. Sørensen, S. G.; Füchtbauer, H. G.; Tuxen, A. K.; Walton, A. S.; Lauritsen, J. V., Structure and Electronic Properties of In Situ Synthesized Single-Layer MoS₂ on a Gold Surface. *ACS Nano* **2014**, *8* (7), 6788-6796.
20. Hall, J.; Pielic, B.; Murray, C.; Jolie, W.; Wekking, T.; Busse, C.; Kralj, M.; Michely, T., Molecular beam epitaxy of quasi-freestanding transition metal disulphide monolayers on van der Waals substrates: a growth study. *2D Materials* **2018**, *5* (2), 025005.
21. Ugeda, M. M.; Bradley, A. J.; Shi, S.-F.; da Jornada, F. H.; Zhang, Y.; Qiu, D. Y.; Ruan, W.; Mo, S.-K.; Hussain, Z.; Shen, Z.-X.; Wang, F.; Louie, S. G.; Crommie, M. F., Giant bandgap renormalization and excitonic effects in a monolayer transition metal dichalcogenide semiconductor. *Nature Materials* **2014**, *13* (12), 1091-1095.
22. Bruix, A.; Miwa, J. A.; Hauptmann, N.; Wegner, D.; Ulstrup, S.; Grønborg, S. S.; Sanders, C. E.; Dendzik, M.; Grubišić Čabo, A.; Bianchi, M.; Lauritsen, J. V.; Khajetoorians, A. A.; Hammer, B.; Hofmann, P., Single-layer MoS₂ on Au(111): Band gap renormalization and substrate interaction. *Physical Review B* **2016**, *93* (16), 165422.
23. Shao, B.; Eich, A.; Sanders, C.; Ngankeu, A. S.; Bianchi, M.; Hofmann, P.; Khajetoorians, A. A.; Wehling, T. O., Pseudodoping of a metallic two-dimensional material by the supporting substrate. *Nature Communications* **2019**, *10* (1), 180.
24. Dendzik, M.; Bruix, A.; Michiardi, M.; Ngankeu, A. S.; Bianchi, M.; Miwa, J. A.; Hammer, B.; Hofmann, P.; Sanders, C. E., Substrate-induced semiconductor-to-metal transition in monolayer WS₂. *Physical Review B* **2017**, *96* (23), 235440.
25. Krane, N.; Lotze, C.; Läger, J. M.; Reece, G.; Franke, K. J., Electronic Structure and Luminescence of Quasi-Freestanding MoS₂ Nanopatches on Au(111). *Nano Letters* **2016**, *16* (8), 5163-5168.
26. Grubišić Čabo, A.; Miwa, J. A.; Grønborg, S. S.; Riley, J. M.; Johannsen, J. C.; Cacho, C.; Alexander, O.; Chapman, R. T.; Springate, E.; Grioni, M.; Lauritsen, J. V.; King, P. D. C.; Hofmann, P.; Ulstrup, S., Observation of Ultrafast Free Carrier Dynamics in Single Layer MoS₂. *Nano Letters* **2015**, *15* (9), 5883-5887.
27. Murray, C.; Jolie, W.; Fischer, J. A.; Hall, J.; van Efferen, C.; Ehlen, N.; Grüneis, A.; Busse, C.; Michely, T., Comprehensive tunneling spectroscopy of quasifreestanding MoS₂ on graphene on Ir(111). *Physical Review B* **2019**, *99* (11), 115434.
28. Albertini, O. R.; Liu, A. Y.; Calandra, M., Effect of electron doping on lattice instabilities in single-layer TaS₂. *Physical Review B* **2017**, *95* (23), 235121.
29. Hall, J.; Ehlen, N.; Berges, J.; van Loon, E.; van Efferen, C.; Murray, C.; Rösner, M.; Li, J.; Senkovskiy, B. V.; Hell, M.; Rolf, M.; Heider, T.; Asensio, M. C.; Avila, J.; Plucinski, L.; Wehling, T.; Grüneis, A.; Michely, T., Environmental Control of Charge Density Wave Order in Monolayer 2H-TaS₂. *ACS Nano* **2019**, *13* (9), 10210-10220.
30. Ugeda, M. M.; Bradley, A. J.; Zhang, Y.; Onishi, S.; Chen, Y.; Ruan, W.; Ojeda-Aristizabal, C.; Ryu, H.; Edmonds, M. T.; Tsai, H.-Z.; Riss, A.; Mo, S.-K.; Lee, D.; Zettl, A.; Hussain, Z.; Shen, Z.-X.; Crommie, M. F., Characterization of collective ground states in single-layer NbSe₂. *Nature Physics* **2016**, *12* (1), 92-97.
31. Chen, Y.; Ruan, W.; Wu, M.; Tang, S.; Ryu, H.; Tsai, H.-Z.; Lee, R.; Kahn, S.; Liou, F.; Jia, C.; Albertini, O. R.; Xiong, H.; Jia, T.; Liu, Z.; Sobota, J. A.; Liu, A. Y.; Moore, J. E.; Shen, Z.-X.; Louie, S. G.; Mo, S.-K.; Crommie, M. F., Strong correlations and orbital texture in single-layer 1T-TaSe₂. *Nature Physics* **2020**, *16*, 218-224.

32. Arnold, F.; Stan, R.-M.; Mahatha, S. K.; Lund, H. E.; Curcio, D.; Dendzik, M.; Bana, H.; Travaglia, E.; Bignardi, L.; Lacovig, P.; Lizzit, D.; Li, Z.; Bianchi, M.; Miwa, J. A.; Bremholm, M.; Lizzit, S.; Hofmann, P.; Sanders, C. E., Novel single-layer vanadium sulphide phases. *2D Materials* **2018**, *5* (4), 045009.
33. Zeller, P.; Günther, S., What are the possible moiré patterns of graphene on hexagonally packed surfaces? Universal solution for hexagonal coincidence lattices, derived by a geometric construction. *New Journal of Physics* **2014**, *16* (8), 083028.
34. Krane, N.; Lotze, C.; Franke, K. J., Moiré structure of MoS₂ on Au(111): Local structural and electronic properties. *Surface Science* **2018**, *678*, 136-142.
35. Fumega, A. O.; Gobbi, M.; Dreher, P.; Wan, W.; González-Orellana, C.; Peña-Díaz, M.; Rogero, C.; Herrero-Martín, J.; Gargiani, P.; Ilyn, M.; Ugeda, M. M.; Pardo, V.; Blanco-Canosa, S., Absence of Ferromagnetism in VSe₂ Caused by Its Charge Density Wave Phase. *The Journal of Physical Chemistry C* **2019**, *123* (45), 27802-27810.
36. Feng, J.; Biswas, D.; Rajan, A.; Watson, M. D.; Mazzola, F.; Clark, O. J.; Underwood, K.; Marković, I.; McLaren, M.; Hunter, A.; Burn, D. M.; Duffy, L. B.; Barua, S.; Balakrishnan, G.; Bertran, F.; Le Fèvre, P.; Kim, T. K.; van der Laan, G.; Hesjedal, T.; Wahl, P.; King, P. D. C., Electronic Structure and Enhanced Charge-Density Wave Order of Monolayer VSe₂. *Nano Letters* **2018**, *18* (7), 4493-4499.
37. Duvjir, G.; Choi, B. K.; Jang, I.; Ulstrup, S.; Kang, S.; Thi Ly, T.; Kim, S.; Choi, Y. H.; Jozwiak, C.; Bostwick, A.; Rotenberg, E.; Park, J.-G.; Sankar, R.; Kim, K.-S.; Kim, J.; Chang, Y. J., Emergence of a Metal-Insulator Transition and High-Temperature Charge-Density Waves in VSe₂ at the Monolayer Limit. *Nano Letters* **2018**, *18* (9), 5432-5438.
38. Coelho, P. M.; Nguyen Cong, K.; Bonilla, M.; Kolekar, S.; Phan, M.-H.; Avila, J.; Asensio, M. C.; Oleynik, I. I.; Batzill, M., Charge Density Wave State Suppresses Ferromagnetic Ordering in VSe₂ Monolayers. *The Journal of Physical Chemistry C* **2019**, *123* (22), 14089-14096.
39. Bonilla, M.; Kolekar, S.; Ma, Y.; Diaz, H. C.; Kalappattil, V.; Das, R.; Eggers, T.; Gutierrez, H. R.; Phan, M.-H.; Batzill, M., Strong room-temperature ferromagnetism in VSe₂ monolayers on van der Waals substrates. *Nature Nanotechnology* **2018**, *13* (4), 289-293.
40. Zhang, H.; Liu, L.-M.; Lau, W.-M., Dimension-dependent phase transition and magnetic properties of VS₂. *Journal of Materials Chemistry A* **2013**, *1* (36), 10821-10828.
41. Ma, Y.; Dai, Y.; Guo, M.; Niu, C.; Zhu, Y.; Huang, B., Evidence of the Existence of Magnetism in Pristine VX₂ Monolayers (X = S, Se) and Their Strain-Induced Tunable Magnetic Properties. *ACS Nano* **2012**, *6* (2), 1695-1701.
42. Isaacs, E. B.; Marianetti, C. A., Electronic correlations in monolayer $\{\mathrm{VS}\}_2$. *Physical Review B* **2016**, *94* (3), 035120.
43. Kamber, U.; Bergman, A.; Eich, A.; Iuşan, D.; Steinbrecher, M.; Hauptmann, N.; Nordström, L.; Katsnelson, M. I.; Wegner, D.; Eriksson, O.; Khajetoorians, A. A., Self-induced spin glass state in elemental and crystalline neodymium. *Science* **2020**, *368* (6494), eaay6757.
44. Hoffmann, S. V.; Søndergaard, C.; Schultz, C.; Li, Z.; Hofmann, P., An undulator-based spherical grating monochromator beamline for angle-resolved photoemission spectroscopy. *Nuclear Instruments and Methods in Physics Research Section A: Accelerators, Spectrometers, Detectors and Associated Equipment* **2004**, *523* (3), 441-453.
45. Kresse, G.; Joubert, D., From ultrasoft pseudopotentials to the projector augmented-wave method. *Physical Review B* **1999**, *59* (3), 1758-1775.
46. Kresse, G.; Furthmüller, J., Efficiency of ab-initio total energy calculations for metals and semiconductors using a plane-wave basis set. *Computational Materials Science* **1996**, *6* (1), 15-50.
47. Perdew, J. P.; Burke, K.; Ernzerhof, M., Generalized Gradient Approximation Made Simple. *Physical Review Letters* **1996**, *77* (18), 3865-3868.
48. Monkhorst, H. J.; Pack, J. D., Special points for Brillouin-zone integrations. *Physical Review B* **1976**, *13* (12), 5188-5192.

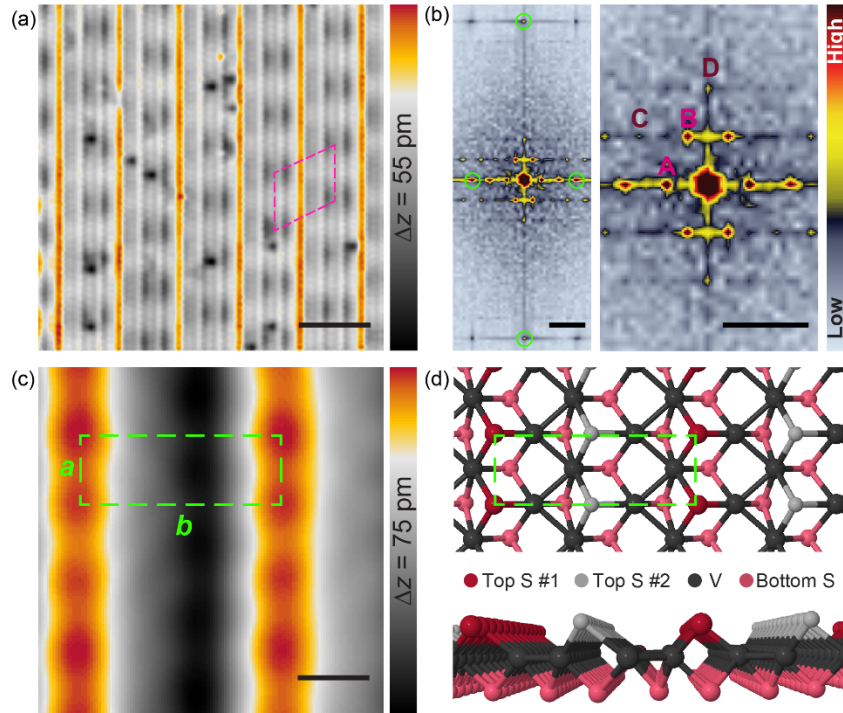


Figure 1. (a) Large scale constant-current STM image of the surface, illustrating the two-fold symmetric atomic lattice of top S atoms, as well as a moiré superstructure caused by the lattice mismatch between V_2S_3 monolayer and Au(111) substrate ($V_s = 1$ V, $I_t = 40$ nA, $T = 1.3$ K, scale bar = 3 nm). (b) Corresponding FFT of the image in (a) (scale bar = 5 nm $^{-1}$), with a close-up view of the center (scale bar = 5 nm $^{-1}$). Green circles in the FFT images highlight the reciprocal lattice points of the atomic lattice; the corresponding real-space unit is drawn in (c). The real space unit cell of the moiré is plotted with dashed magenta lines in (a). (c) Atomically resolved constant-current image of ML V_2S_3 revealing the atomic unit cell ($V_s = 3$ mV, $I_t = 1$ nA, $T = 1.3$ K, scale bar = 300 pm). (d) Structural model of ML V_2S_3 /Au(111) (adapted from ³²).

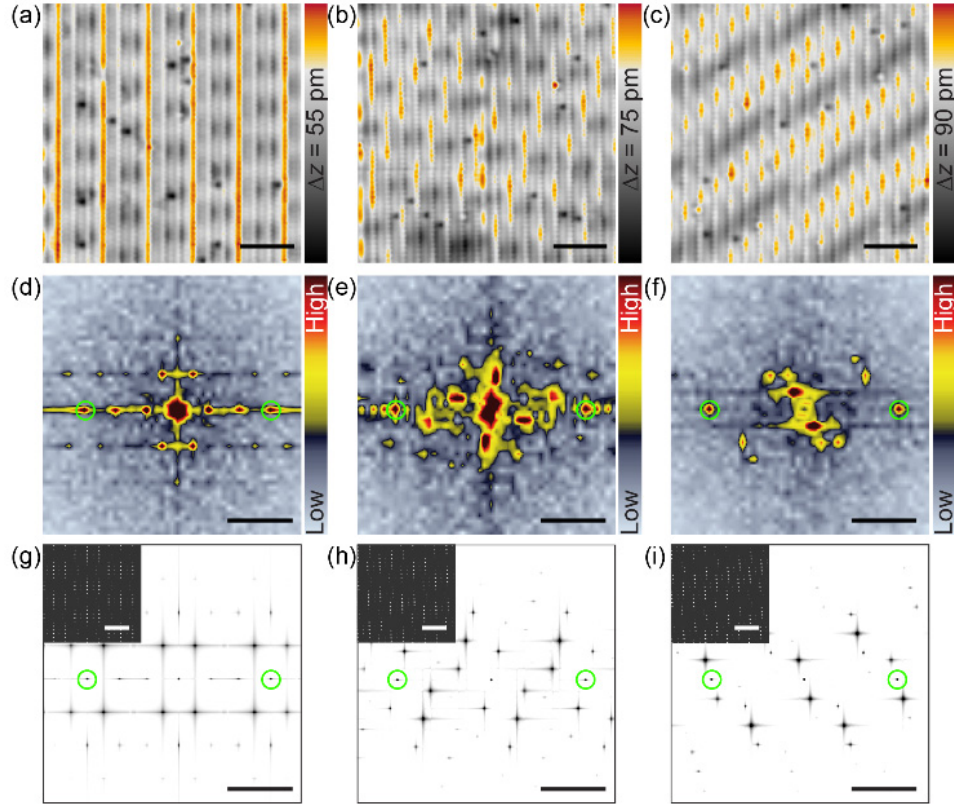


Figure 2. (a-c) Atomically resolved constant-current STM images showing identical atomic lattices with different moiré structures resulting from different rotation angles between the V₂S₃ layer and Au(111) substrate ($\theta = 0^\circ$, 1.3° , and 4.2° with respect to $\langle 110 \rangle$) ($V_s = 1$ V, $I_t = 40$ nA, $T = 1.3$ K, scale bar = 3 nm). (d-f) FFTs of the respective images in (a-c) (scale bar = 5 nm^{-1}). (g-i) FFTs of simulated moiré images with the same scale bar. Insets show the simulations in real space (scale bar = 2 nm). Green circles highlight reciprocal lattice points of V₂S₃.

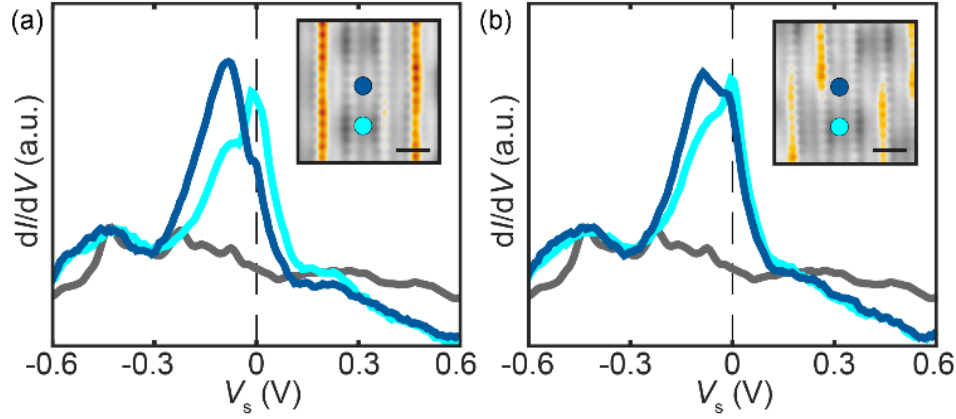


Figure 3. dI/dV spectra acquired at different positions (indicated in blue in the insets) of the moiré superstructure of monolayer V_2S_3 on Au(111), for (a) $\theta = 0^\circ$ and (b) $\theta = 1.3^\circ$. The peak in the dI/dV is observed at all probed positions of the moiré unit cell, but with variations in energy. The surface state of Au(111) is shown for reference (gray). (Stabilization bias (V_{stab}) = 1.5 V, stabilization current (I_{stab}) = 600 pA, modulation bias (V_{mod}) = 1 mV, $T = 1.3$ K; insets: $V_s = 1$ V, $I_t = 40$ nA, $T = 1.3$ K, scale bar = 1 nm).

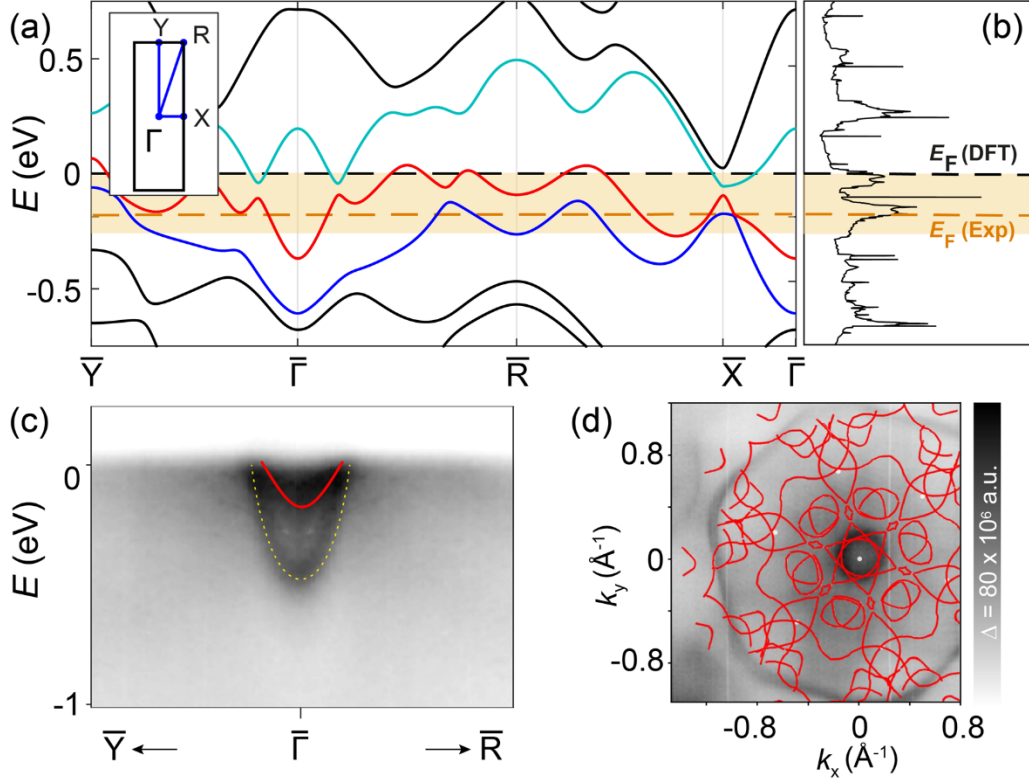


Figure 4. (a) Band structure of V_2S_3 along the high-symmetry path shown in the inset. The black dashed line indicates the DFT Fermi energy, while the Fermi energy determined by comparison with the ARPES measurements is marked by an orange dashed line. (b) Total density of states (DOS). (c) Comparison of the band dispersion around $\bar{\Gamma}$ measured by ARPES with DFT. Yellow dashed line illustrates the surface state of Au(111). (d) Fermi contour calculated from DFT taking into account the three rotational domains, in comparison with the ARPES measurements.

Supporting Information

Moiré-induced electronic structure modifications in monolayer V₂S₃ on Au(111)

Umut Kamber¹, Sahar Pakdel², Raluca-Maria Stan², Anand Kamlapure¹, Brian Kiraly¹, Fabian Arnold², Andreas Eich¹, Arlette S. Ngankeu², Marco Bianchi², Jill A. Miwa², Charlotte E. Sanders³, Nicola Lanata², Philip Hofmann², Alexander A. Khajetoorians^{1*}

1. *Institute for Molecules and Materials, Radboud University, Nijmegen 6525AJ, The Netherlands*
2. *Department of Physics and Astronomy, Interdisciplinary Nanoscience Center, Aarhus University, 8000 Aarhus C, Denmark*
3. *Central Laser Facility, STFC Rutherford Appleton Laboratory, Harwell, Didcot OX11 0QX, United Kingdom*

1. Moiré simulations

We simulated the expected moiré patterns in MATLAB by multiplying sinusoidal functions representing each of the atomic lattices. The Au(111) surface in Figure S1a is generated using three sinusoidal functions with the same wavelength, rotated 120° with respect to each other, as explained in Zeller *et.al*¹. Similarly, top sulfur layer of V₂S₃ is generated using the function:

$$f_S(\mathbf{x}, \mathbf{y}) = \cos(2\mathbf{k}_b\mathbf{x}) + \cos(\mathbf{k}_b\mathbf{x}) + \cos(\mathbf{k}_a\mathbf{y})$$

where $k_a = 2\pi/a$ and $k_b = 2\pi/b$. The corrugation of both f_S and f_{Au} functions were chosen to be between 0 and 1. Both lattices were simulated on a 600nm × 600nm grid, with 2048 pixels in each direction. The real space simulations of both individual lattices, and their corresponding FFTs are shown in Figure S1. The resulting moiré pattern was calculated as a product of two lattices with orders n and m ;

$$M = f_S^n \times f_{Au}^m$$

For the moiré superstructure shown in Figure S1c, and in all the simulations shown in the main text, 6th order functions are used, in order to capture all possible higher-order modes.

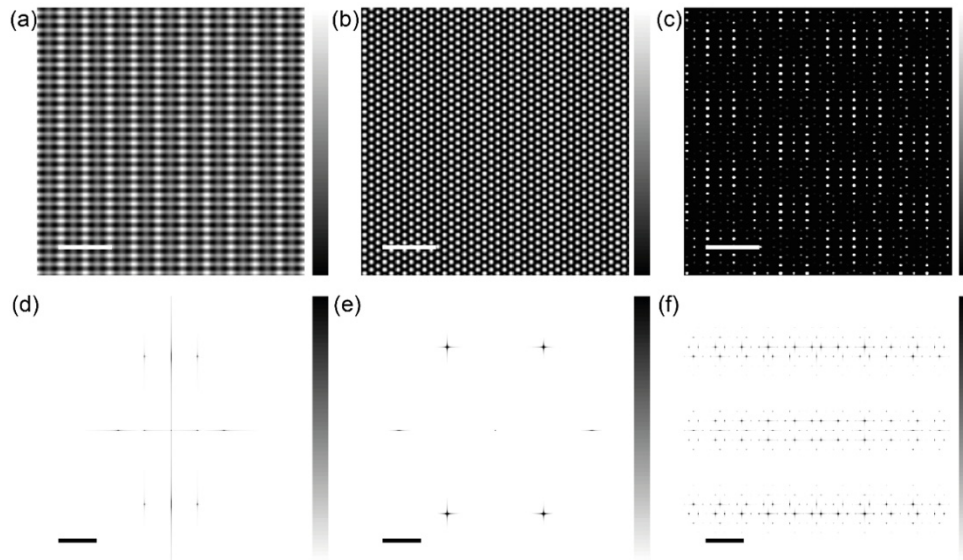


Figure S1. Simulations in real space for (a) top sulfur layer of V₂S₃ monolayer, (b) Au(111) surface, and (c) resulting moiré pattern ($n = m = 6$, scale bar = 2 nm). (d-f) Corresponding FFTs of the images above (scale bar = 10 nm⁻¹).

2. Real space characterization

A high-resolution STM image in Figure S2a shows the morphology of the sample surface. Elongated V₂S₃ islands with moiré superstructure, as well as the herringbone reconstruction of the clean Au(111) surface,

can be clearly seen. The figure illustrates that a majority of the islands are oriented to yield the $\theta = 0^\circ$ moiré superstructure (where the \mathbf{a} direction of V_2S_3 and $\langle 110 \rangle$ direction of the substrate are parallel). Furthermore, these domains form with three different rotations, consistent with the three-fold symmetry of the Au(111).

Atomically resolved STM images at two different biases are shown in Figure S2b,c. A distinct feature with a longer-range modulation can be seen in the real space STM images in Figure S2b: the S rows between moiré minima (red-yellow rows) have higher apparent height than their neighbors. Following the moiré periodicity, these rows repeat every three-unit cells along the \mathbf{b} direction, thus, they correspond to the A-point in reciprocal space.

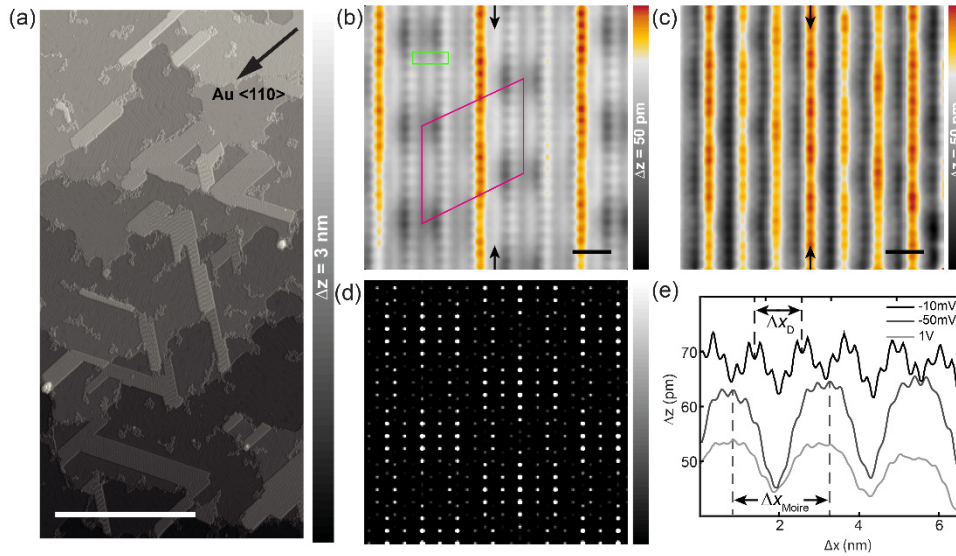


Figure S2. (a) Large scale STM image of the surface ($V_s = -1$ V, $I_t = 100$ pA, $T = 1.3$ K, scale bar = 100 nm). (b) Atomically resolved STM image of the V_2S_3 island surface measured at $V_s = 1$ V ($I_t = 40$ nA, $T = 1.3$ K, scale bar = 1 nm). (c) The exact same area is measured at $V_s = -10$ mV. (d) Real space moiré simulations for the moiré superstructure in (b). (e) Line profiles extracted along the sulfur row (marked with black arrows in (b, c)) from the images measured at different biases.

The exact same area is measured at $V_s = -10$ mV (Figure S2c), showing that the contrast of the moiré superstructure disappears at low biases, while another longer-range modulation appears. Line profiles along the sulfur row were extracted from the images in Figure S2b,c and shown in Figure S2e, illustrating the apparent height modulations of individual periodicities together with atomic corrugation. The additional modulation observed at low bias imaging has a periodicity matching the one of the higher-order modes of

the moiré superstructure (indicated as D-point in Figure 1). Real space simulations for the same moiré superstructure are shown in Figure S2d.

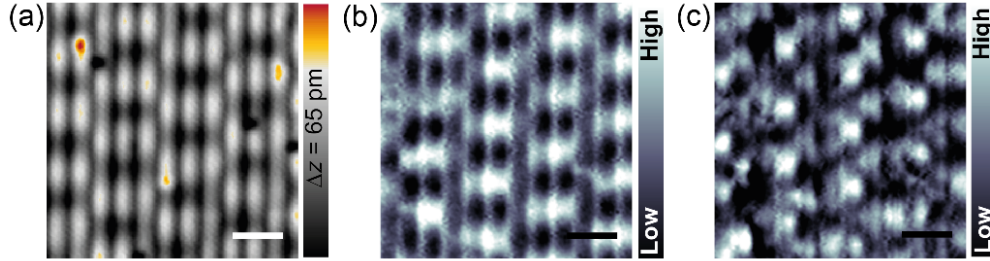


Figure S3. (a) Constant-current STM image ($V_s = -0.8$ V, $I_t = 200$ pA, $T = 1.3$ K, scale bar = 2 nm). Spatially dependent differential conductance maps of the same area measured at (b) $V_s = -50$ mV and (c) $V_s = -10$ mV ($V_{\text{mod}} = 2$ mV, $I_t = 200$ pA, $T = 1.3$ K, scale bar = 2 nm).

In order to capture spatial variations in the LDOS, we acquired differential conductance maps using a lock-in detection technique (Figure S3) and tunneling spectra on along the direction of atomic sulfur rows across multiple moiré units (Figure S4). A constant-current image of the surface is shown in Figure S3a, illustrating the atomic top sulfur rows as well as the moiré superstructure. Differential conductance maps were acquired in the same area at two different biases ($V_s = -50$ mV in Figure S3b and $V_s = -10$ mV in Figure S3c), where characteristic changes were observed in tunneling spectra shown in the main text (Figure 3 and Figure S4). As a result of the variations in LDOS within the moiré unit, seen in the shifting dI/dV peak at approximately -100 mV in Figure S4, the differential conductance maps show a complicated real-space structure (Figure S3).

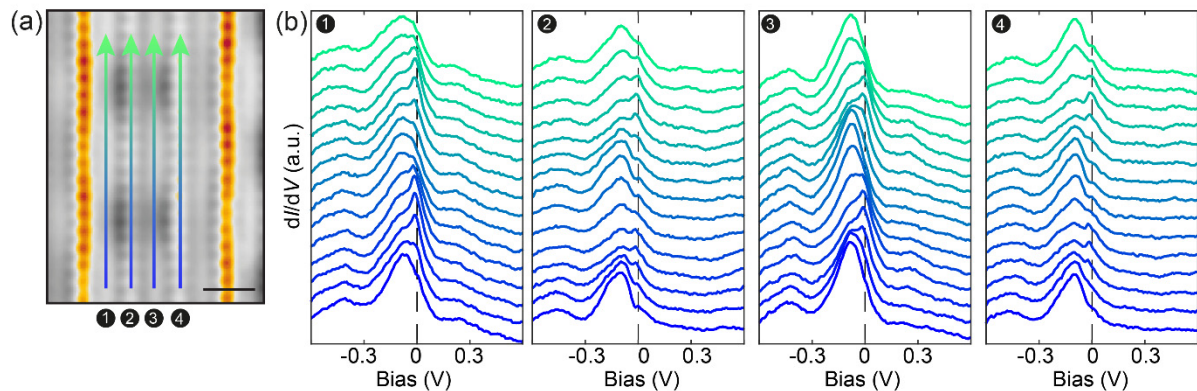


Figure S4. (a) Constant-current STM image ($V_s = 1$ V, $I_t = 40$ nA, $T = 1.3$ K, scale bar = 1 nm). (b) dI/dV spectra acquired at different positions along atomic sulfur rows (indicated by arrows and numbers) on the surface ($V_{\text{stab}} = 1.5$ V, $I_{\text{stab}} = 600$ pA, $V_{\text{mod}} = 1$ mV, $T = 1.3$ K).

3. Orbital decomposition

Projections of the total DOS onto each of the d -orbitals of vanadium is shown in Figure S5. The figure reveals that the character of the DOS near the experimental Fermi energy has a strong contribution from the out-of-plane V d -orbitals.

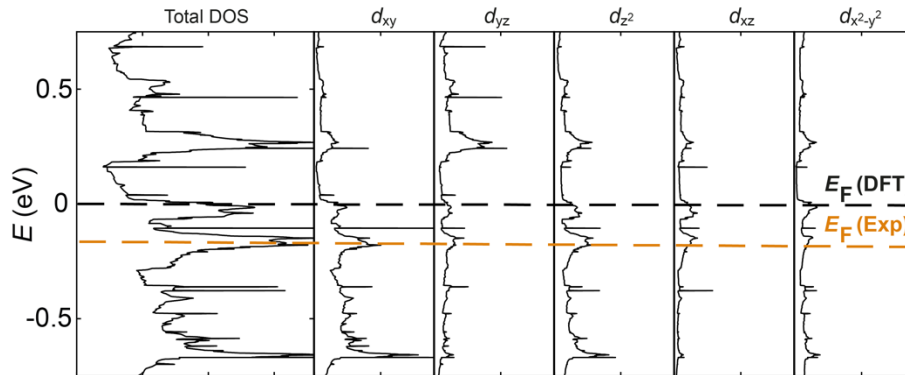


Figure S5. Total DOS and orbitally resolved contributions from the d -orbitals of vanadium.

4. Comparison between ARPES and DFT calculations

Here we discuss the behavior of the DFT and ARPES energy contours at different energies. In particular, in Figure S6, we compare the calculated DFT energy contours to the ARPES energy contours at two different energies, namely at the Fermi level $E_F(\text{exp})$ and at $E_F(\text{exp}) - 125$ meV. Note that, besides effectively shifting the Fermi level, the V_2S_3 monolayer possibly hybridizes with the Au(111) substrate. Such hybridization effects are not included in these DFT calculations. Furthermore, since the ARPES intensity is highly dependent on matrix elements, not all features predicted by theory are visible experimentally. However, as explained below, some of the main qualitative features of the constant energy contours are consistent with the theoretical predictions, both at the Fermi level and at $E_F(\text{exp}) - 125$ meV.

In Figure S6, we inspect the behavior of the band structure as a function of the energy, focusing on the V- $3d$ pockets around the $\bar{\Gamma}$ point and its second-order repetitions. Panels (c) and (g) show the DFT contributions to the constant energy contours originating from a single rotational domain (the one corresponding to the yellow rectangle in panel i), while panels (d) and (h) show the contributions from all rotational domains, simultaneously. At the first $\bar{\Gamma}$ point, the Au(111) surface state dominates the ARPES

intensity in the constant energy contours. However, the behavior of the ARPES V-3d pockets can be observed very clearly at the second-order Brillouin-zone repetitions of the V_2S_3 $\bar{\Gamma}$ point (marked by white dots in panels (b-d, f-h) of Figure S6), where the Au(111) background intensity is relatively weak. By comparing the panels (b) and (f), it is clear that the ARPES signatures narrow down around the indicated white dots when going from the $E_F(\text{exp})$ to $E_F(\text{exp}) - 125$ meV. Based on the comparison in the panels (d) and (h), we attribute this behavior to the fact that the V-3d pockets around the $\bar{\Gamma}$ point become smaller as the absolute energy is reduced.

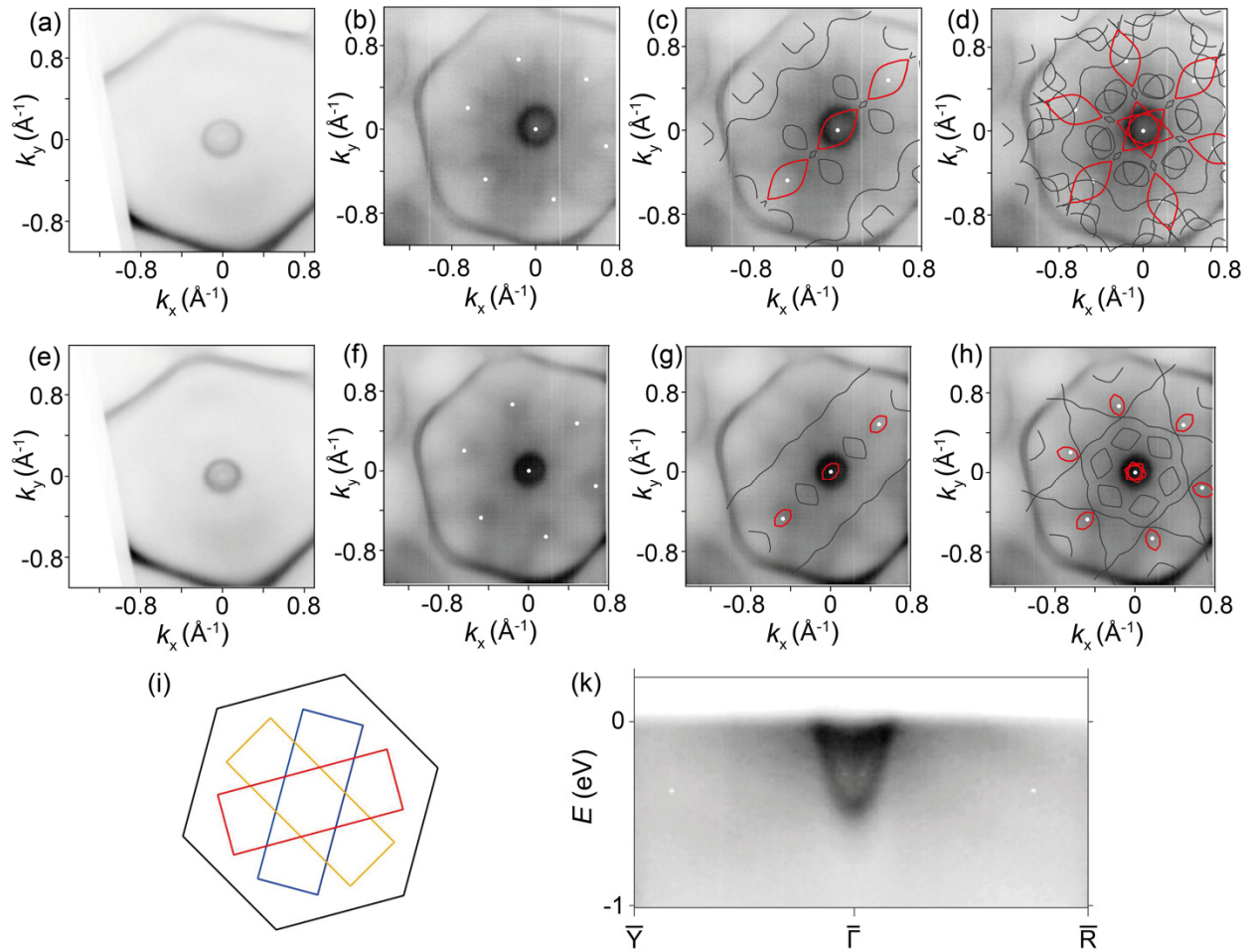


Figure S6. ARPES Fermi contour of (a) bare Au(111), and (b) $V_2S_3/Au(111)$ at the Fermi level. (c-d) Fermi contour of the free-standing monolayer V_2S_3 calculated with DFT at $E_F(\text{Exp})$, in comparison with ARPES data from (b). ARPES constant energy contours of (e) bare Au(111), and (f) $V_2S_3/Au(111)$ at -125 meV. (g-h) Constant energy contours of the free-standing monolayer V_2S_3 calculated with DFT at $E_F(\text{Exp}) = -125$ meV, in comparison with ARPES. In panels (c, g) only the contribution of one of the rotational domains is shown (yellow rectangle in panel i). (i) Schematics of the surface BZ of Au(111) and the BZs of the three rotational domains of V_2S_3 monolayer, with orientation consistent with panels. (k) Band dispersion

measured by ARPES on $V_2S_3/Au(111)$, taken from Fig. 4. The white dots are referenced in the discussion above.

5. Electronic susceptibility calculations

To investigate the interplay between electronic and orbital degrees of freedom, we calculated the electronic susceptibility $\chi(\mathbf{q})$, as peaks in its real part $\chi'(\mathbf{q})$ and imaginary part $\chi''(\mathbf{q})$ (nesting function) are often associated with structural instabilities. Within the so-called “constant matrix element approximation”^{2,3}, $\chi'(\mathbf{q})$ is given by;

$$\chi'(\mathbf{q}) = \sum_{\mathbf{k}} \frac{f(\epsilon_{\mathbf{k}}) - f(\epsilon_{\mathbf{k}+\mathbf{q}})}{\epsilon_{\mathbf{k}} - \epsilon_{\mathbf{k}+\mathbf{q}}}$$

(often referred to as the Lindhard function), where \mathbf{k} belongs to the BZ, \mathbf{q} is a generic reciprocal-space vector, f is the Fermi function and $\epsilon_{\mathbf{k}}$ is the band energy.

The results of our calculations are summarized in Figure S7. Both the electronic susceptibility $\chi'(\mathbf{q})$ and the nesting function $\chi''(\mathbf{q})$, calculated at the theoretically estimated E_F (DFT) for the free-standing V_2S_3 monolayer, display a peak very close to one of the second-order points of the $\theta = 0^\circ$ moiré superstructure (indicated as the C-point in Figure S7 and in Figure 1). As these calculations only account for the free-standing monolayer, the modifications in the band structure induced by the moiré superstructure or the hybridization with the substrate are expected to yield considerable changes in the electronic susceptibility.

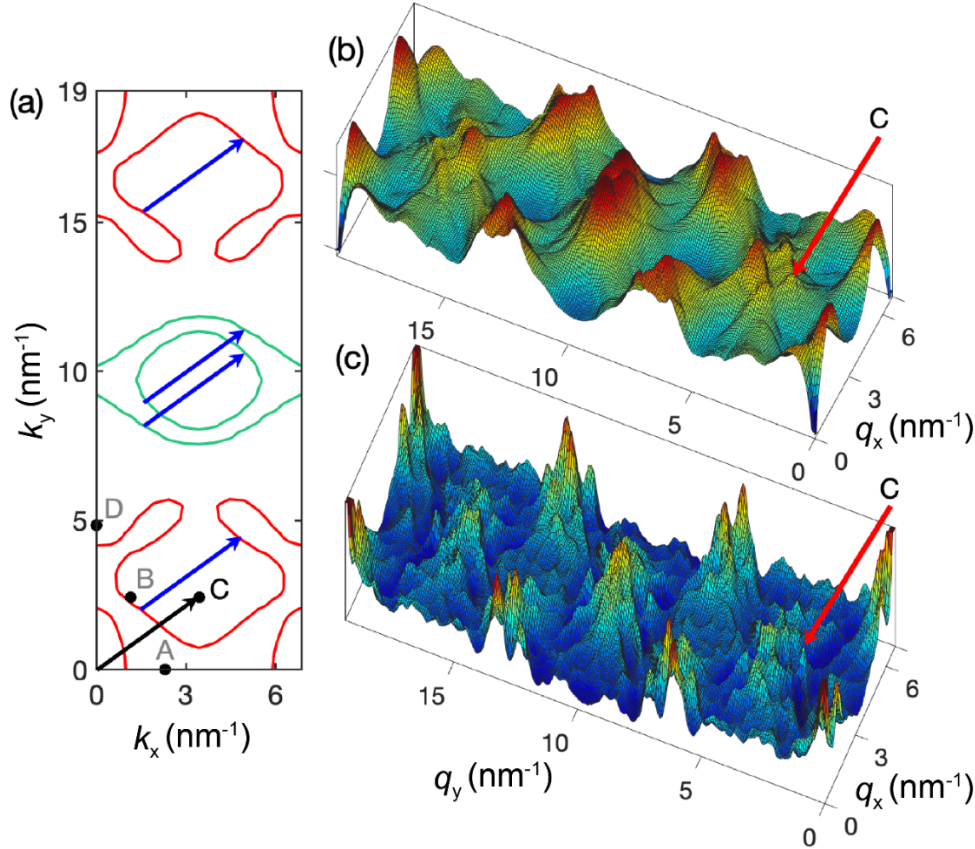


Figure S7. (a) Fermi contour of free-standing monolayer V_2S_3 calculated with DFT. The reference Fermi energy is set to the value E_F (DFT) determined theoretically, see the black dashed line in Figure 4. The colors of the Fermi contour lines correspond to the bands shown in Figure 4. The black dots correspond to the reciprocal-space points indicated in Figure 1. (b) Real part of the electronic susceptibility $\chi'(\mathbf{q})$. (c) Imaginary part of the electronic susceptibility (nesting function) $\chi''(\mathbf{q})$. The Fermi-surface nesting (indicated by arrows in panel (a)) responsible for the peaks in $\chi(\mathbf{q})$ (panels (b, c)) coincides with the reciprocal higher order moiré point C.

Supplementary References

1. Zeller, P.; Günther, S., What are the possible moiré patterns of graphene on hexagonally packed surfaces? Universal solution for hexagonal coincidence lattices, derived by a geometric construction. *New Journal of Physics* **2014**, *16* (8), 083028.
2. Gupta, R. P.; Freeman, A. J., Role of matrix elements in the theoretical determination of generalized susceptibilities in metals. *Physical Review B* **1976**, *13* (10), 4376-4386.
3. Pickett, W. E.; Allen, P. B., Superconductivity and phonon softening. III. Relation between electron bands and phonons in Nb, Mo, and their alloys. *Physical Review B* **1977**, *16* (7), 3127-3132.